DOI: 10.1002/adma.200601187

Carbon Nanotubes as Optical Antennae**

By *Krzysztof Kempa,* Jakub Rybczynski, Zhongping Huang, Keith Gregorczyk, Andy Vidan, Brian Kimball, Joel Carlson, Glynda Benham, Yang Wang, Andrzej Herczynski,* and *Zhifeng Ren**

Light scattering from an array of aligned multiwall carbon nanotubes (MWCNTs) has previously been investigated,[1,2] and shown to be consistent with that from an array of antennae. Two basic antenna effects have been demonstrated: 1) the polarization effect, which suppresses the response of an antenna when the electric field of the incoming radiation is polarized perpendicular to the dipole antenna axis, and 2) the antenna-length effect, which maximizes the antenna response when the antenna length is a multiple of the radiation half wavelength in the medium surrounding the antenna. In these previous experiments a random nanotube array was chosen to eliminate the intertube diffraction effects. In this communication, we provide compelling evidence of the antenna action of an MWCNT, by demonstrating that its directional radiation characteristics are in an excellent and quantitative agreement with conventional radio antenna theory and simulations.

According to conventional radio antenna theory,[3–6] a simple "thin" wire antenna (a metallic rod of diameter d and length $l \gg d$) maximizes its response to a wavelength λ when $l = m\lambda/2$, where m is a positive integer. Thus, an antenna acts as a resonator of the external electromagnetic radiation. An antenna is a complex boundary value problem; it is a resonator for both the external fields, and the currents at the antenna surface. In a long radiating antenna, a periodic pattern of current distribution is excited along the antenna, synchronized with the pattern of fields outside. The current pattern consists of segments, with the current direction alternating from segment to segment. Thus, a long antenna can be viewed as an antenna array consisting of smaller, coherently driven antennae (segments) in series. Therefore, the resulting radiation pattern, as a function of the angle with respect to the antenna axis, consists of lobes of constructive interference, separated by radiation minima due to destructive interference.

Consider a simple antenna as shown in Figure 1a. The radiation pattern produced by this antenna is rotationally symmetric about the z axis. For a center-fed antenna, or one excited by an external wave propagating perpendicular to the antenna axis (i.e., with the glancing angle $\theta_i = 90°$), the pattern is also symmetric with respect to the x–y plane. For an antenna excited by an incoming wave propagating at an angle ($\theta_i < 90°$), the relative strengths of the radiation lobes are expected to shift towards the specular direction. This follows from a qualitative argument based on the single-photon scattering picture, and conservation laws for scattered photons from an antenna. Since such scattering is elastic, the energy of each scattering photon $\hbar\omega$ (where $\hbar$ is the reduced Planck constant and ω is the angular frequency) and its total momentum $\hbar k = \hbar|\boldsymbol{k}_i| = \hbar|\boldsymbol{k}_s|$ (where k is the wave number, $\boldsymbol{k}_i$ is the incident wave vector, and $\boldsymbol{k}_s$ is the scattered wave vector) must be conserved. Due to the cylindrical symmetry, $\hbar K$, the length of the momentum vector component perpendicular to the antenna, must also be conserved. Thus, the momentum components parallel to the antenna for the incoming, and scattered photons, $\hbar k_{\parallel(s)}$ and $\hbar k_{\parallel(i)}$ respectively, satisfy the following condition $k^2_{\parallel(i)} = k^2 - K^2 = k^2_{\parallel(s)}$, or finally $k_{\parallel(s)} = \pm k_{\parallel(i)}$. This immediately leads to a formula for the angle of scattering $\theta_s = 180° - \theta_i$, since for a "thin" antenna with diameter $d \ll l$, the back scattering is suppressed, and therefore the negative sign is unlikely. Thus, scattering is dominated by the *specular* reflection. We have confirmed this effect, by measuring the scattered microwave radiation from a simple wire antenna; the forward radiation was about one order of magnitude more intense than for the backward scattered wave.

To complete the preliminary antenna studies, we performed computer simulations[7] of the detailed antenna response to an external plane wave. Figure 1b shows a polar coordinate plot of the radiation pattern (field intensity versus θ), in the y–z plane, from a thin antenna ($d = 0.001l$) with $l = 7\lambda$. The incoming wave of fixed wavelength λ, struck the antenna at different incidence angles $\theta_i = 30°$, 45°, and 60°. This produced radiation patterns dominated by lobes at $\theta_s = 180 - \theta_i = 150°$, 135°, and 120°, respectively: the scattering was dominated by the specular reflection with respect to the 90° line, in agreement with the simple analysis above. Due to cylindrical symmetry in the x–y plane, the response was mirror-image symmetric about the z axis in the x–z plane. The dependence of

[*] Prof. K. Kempa, Prof. Z. F. Ren, Dr. J. Rybczynski, Dr. Y. Wang, Prof. A. Herczynski
Department of Physics, Boston College
Chestnut Hill, MA 02467 (USA)
[redacted]
Z. Huang
NanoLab, Inc.
Newton, MA 02135 (USA)
K. Gregorczyk, A. Vidan, Dr. B. Kimball, J. Carlson
US Army Research Development and Engineering Command
Natick Soldier Center
Natick, MA 01760 (USA)
G. Benham
MegaWave Corporation
Boylston, MA 01505 (USA)

[**] This work is partly supported by the US Army Natick Soldier Systems Center under the grant DAAD16-03-C-0052 and partly by NSF NIRT 0304506.

© 2007 WILEY-VCH Verlag GmbH & Co. KGaA, Weinheim

WILEY InterScience

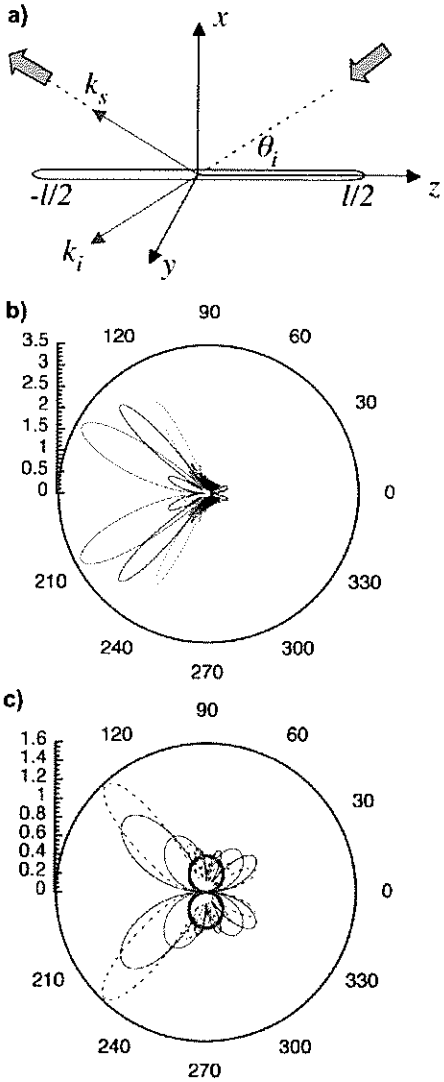

Figure 1. The geometry of the antenna-radiation interaction (a). Bold arrows ($\mathbf{k}_i$ and $\mathbf{k}_s$) represent the wave vectors for incident and scattered waves, respectively. A polar-coordinate plot of the radiation pattern (field intensity versus angle θ), in the y–z plane, from a thin antenna ($d = 0.001l$) with $l = 7\lambda$ (b). The incoming wave of fixed frequency (and λ), strikes the antenna at different incidence angles $\theta_i = 30°$, 45°, and 60°. There is cylindrical symmetry in the x–y plane, and thus the response is mirror-image symmetric about the z-axis in this picture. The dependence of the radiation pattern on the antenna length (c). The incidence angle is $\theta_i = 45°$. The thick solid line is for $l = \lambda/2$, the medium-thick solid line for $l = \lambda$, the thin solid line for $l = 2\lambda$, and the dashed line for $l = 4\lambda$.

the radiation pattern on the antenna length is illustrated in Figure 1c. In this case, the incidence angle was kept constant ($\theta_i = 45°$), but the antenna length was varied: $l = \lambda/2$, λ, 2λ, and 4λ. The corresponding radiation patterns were displayed using a decreasing line thickness (and decreasing darkness of shading) with increasing antenna length (the dashed line is for $l = 4\lambda$). They demonstrate the evolution towards the specular pattern as the antenna length increases, and the corresponding suppression of the lobes for back-scattered waves. Note that for $l = \lambda/2$ (bold line), the radiation has a maximum in the x–y plane (i.e., no specular reflection). This is obvious, since only one current segment was possible when the antenna was one half wavelength long, and thus no interference could occur to produce a specular enhancement.

These preliminary studies involving conventional, macroscopic antennae set the stage for the subsequent studies of the radiation patterns in MWCNTs. In an earlier work,[1] we have demonstrated two basic antenna effects in dense arrays of MWCNTs. First, the polarization effect shows enhancement of the scattering for light polarized parallel to the nanotubes. Second, the length effect appears as an enhancement of the scattering for light with a wavelength satisfying the condition $l = m\lambda/2$. The MWCNTs have been shown to be metallic, with conductivities comparable to those of Cu or Au.[1] The MWCNTs used in previous work,[1] and in the present study, are "bamboo"-type graphene cylindrical structures, with large diameters (80–200 nm). They consist of multiple cylindrical graphene sheets, with the innermost segments forming enclosed compartments (see Fig. 2). Thus, these MWCNTs are expected to have electromagnetic responses similar to those of metallic nanowires, and certainly not of single-wall carbon nanotubes.[8–12] In particular, because of their large diameter

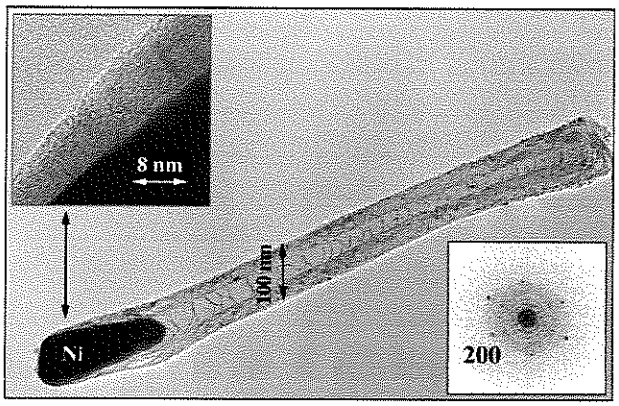

Figure 2. A transmission electron microscopy (TEM) image of a single MWCNT detached from the substrate. The "bamboo" structure of the enclosed compartments is clearly visible. A catalytic Ni nanoparticle remained embedded at the tip of the nanotube. Inset (top-left) shows well-graphitized graphene sheets at the location adjacent to catalyst particle indicated by the arrow. The inset (bottom-right) shows the electron diffraction pattern of the nanotube.

and high plasma frequency (about 6 eV), MWCNTs can support marginally retarded surface waves (plasmon polaritons), which are essentially identical to those in conventional antennae.[8] In order to eliminate the internanotube interactions, the random arrays of MWCNTs in the present work had a large intertube separation ($L \gg \lambda$).

The experimental setup used to demonstrate the optical antenna action in detail is shown in Figure 3a. The laser beam

 © 2007 WILEY-VCH Verlag GmbH & Co. KGaA, Weinheim

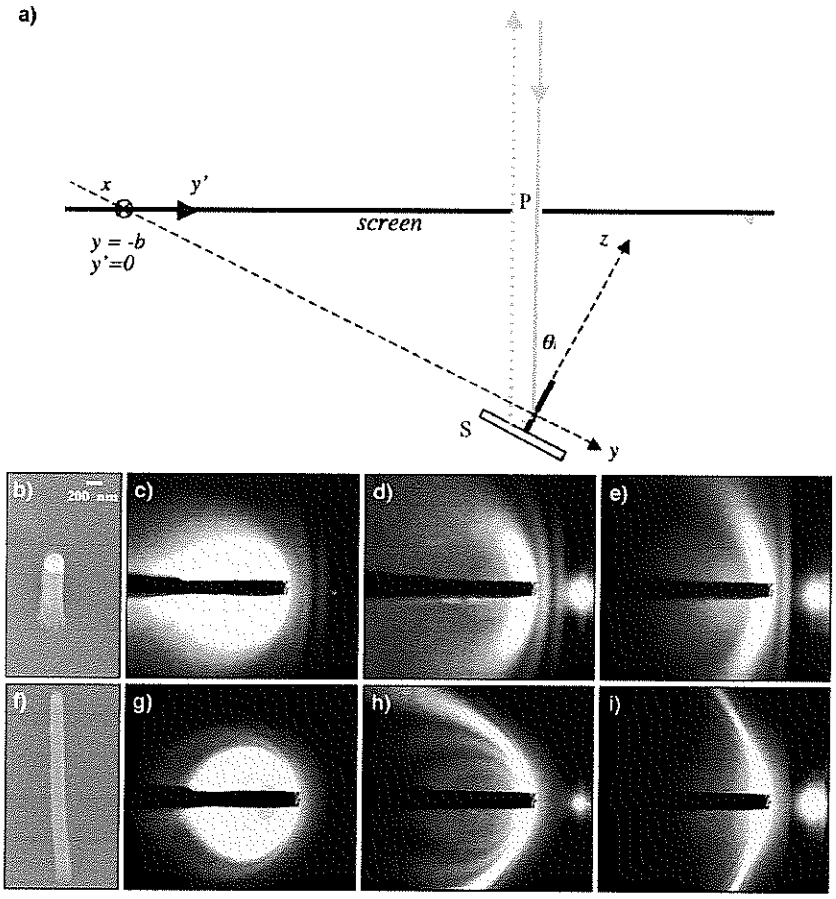

Figure 3. The experimental setup for the demonstration of the optical-antenna action (a). An image of the short nanotube ($l \sim 850$ nm) taken at a 45° tilt angle of the sample with respect to the nanotube axis (b). Images of the laser beam scattered from the array of corresponding nanotubes taken at incident angles of 30° (c), 40° (d), and 50° (e). The image of the long nanotube ($l \sim 3.5$ μm) taken at a 30° tilt angle (f). Images of the laser beam scattered from the array of corresponding nanotubes taken at incident angles of 30° (g), 40° (h), and 50° (i).

entered the measurement area through a hole in a screen (P), with a diameter larger than the diameter of the laser beam, and scattered from the sample (S). The nanotubes (nanoantennae) were at an angle θ_i to the incoming beam. The reradiated (scattered) light projected an image of the radiation pattern onto the screen. Since the scattered radiation consisted of cones of the intensity maxima (lobes), the image on the screen was that of conic sections (ellipses, parabolas, or hyperbolas), as the screen "cut" through the cones of the lobe maxima. For a hypothetical single antenna, suspended without a substrate, the most intense would be the cone of the specular reflection at $\theta_s = 180° - \theta_i$, and thus the corresponding conic cross-section would dominate the projection onto the screen. However, since the nanotubes were grown on a Cr-coated, semi-transparent glass substrate (i.e., they were grounded), the radiation pattern was essentially symmetric about the x–y plane (forward rays in Fig. 3a are not shown), as the forward scattered radiation was mirror-reflected by the substrate back to the half-space above the substrate surface. This is illustrated in Figure 3a by the dashed line, representing the specularly reflected beam (from the antenna and substrate). Thus, a strong mirror image of the specular cone should be also visible at $\theta_s = \theta_i$, that is, it should coincide on the screen with the entry spot of the laser beam (hole).

A simple analysis shows that the formula for the lines observed on the screen is

$$Y = \{-B \pm \sqrt{B2 + 4A(1 + X2)}\}/2A \quad (1)$$

where

$$A = \cos^2\theta_i(\tan^2\theta_i \tan^2\theta_s - 1) \quad (2)$$

and

$$B = 2\cos\theta_i \quad (3)$$

and the reduced coordinates are $Y = y'/b$ and $X = x/b$, and where x and y' are the coordinates along the screen, and b is the distance from the sample center to the screen, as measured along the sample surface (see Fig. 3a). For a fixed θ_i, there is a series of curves, given by Equation 1, each corresponding to a given value of the lobe angle θ_s (the angle at which there is a maximum light intensity for a given lobe). Figure 3 also shows images of the scattering lobes on the screen for three angles of incidence: 30° (c), 40° (d), and 50° (e), for a sample with nanotubes of $l = 3.5$ μm. Figure 3g, 3h, and 3i show similar images for a sample with nanotubes of $l = 850$ nm. The very left scanning electron microscopy (SEM) images show individual nanotubes from the corresponding arrays (Fig. 3b and f).

Figure 4 demonstrates the effects of array density on the scattering. A laser beam illuminated a small area (1 mm^2) of the sample with a MWCNT array, and the scattered light was projected onto a screen. In Figure 4a the low-density array ($L \gg \lambda$) was used, and a characteristic ring structure appeared on the screen. The rings corresponded to the scattering lobes, as was explained above. In Figure 4b, the high-density array ($L \ll \lambda$) was used, and the lobe pattern disappeared. This is a result of strong diffusive scattering, triggered by the near-field interantenna interactions, which obscured the multilobe structure. Indeed, detailed analysis of scattering from this array showed that a faint single ring, corresponding to the main lobe, was still visible. Insets show SEM images of the respective arrays, at the same scale.

© 2007 WILEY-VCH Verlag GmbH & Co. KGaA, Weinheim

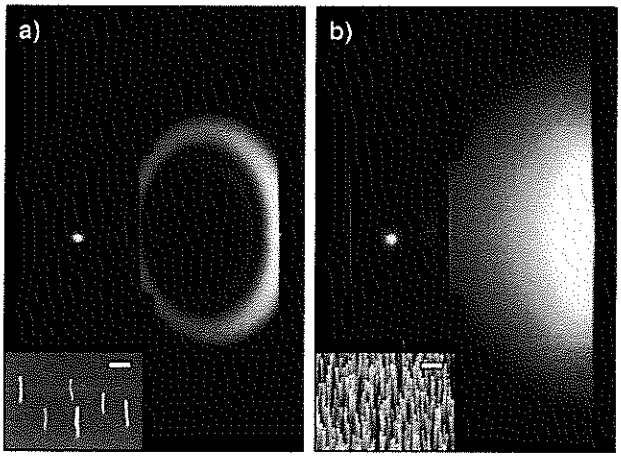

Figure 4. Laser-beam scattering from MWCNT arrays of different density. a) A low-density array ($L \gg \lambda$), and b) a high-density array ($L \ll \lambda$). Insets show SEM images of the corresponding arrays, at the same magnification. Horizontal bars of the insets are 2 μm long.

Figure 5 is the central result of this work. It compares directly the calculated radiation patterns (maps), with those obtained from the experiment. For clarity, results for only two distinctly different nanotubes are shown. The top panels (a, d) show the experimental maps: patterns of the scattered light ($\lambda = 543.5$ nm) on the screen in the configuration of Figure 3a, for $\theta_i = 40°$. The left panel (a) is for the sample with nanotubes of median length $l = 850$ nm, and the right (d) for $l = 3.5$ μm. The middle panels (b, e) in Figure 5 show the calculated maps using Equation 1, with each line obtained from the lobe angles θ_s for a *grounded* antenna of corresponding length. Whereas the longer nanotubes, with $d \ll l$, could indeed be simulated by a "thin" antenna of length $l = 3.5$ μm $= 6.5\lambda$, the shorter nanotubes, which according to Figure 3b have $d \approx 0.3l$, were not "thin" antennae. However, such a "thick" antenna could still be described using "thin" antenna calculation, but with an adjusted "effective" antenna length. We estimate this effective length by extrapolating the results of the calculation for a "thick" ellipsoidal antenna.[13,14] This yields $l' \approx 1.23\,l = 1064$ nm $= 2\lambda$. Each lobe's angular width and its relative intensity, was only very approximately indicated in the middle panels (b, e) by the corresponding line width and brightness. These parameters could be quantitatively assessed by comparison with the corresponding antenna radiation patterns shown in the bottom panels (inset of c, and f). Each pattern was determined using an equivalent *free-standing* antenna, with length twice that of the corresponding *grounded* antenna.[15,16] These patterns, in turn, were used to obtain the lobe angles for the corresponding middle-panel maps in Figure 5.

The experimental and simulated maps (top and middle panels in Fig. 5, respectively) were essentially identical, including the relative intensity of the light maxima, and the width of the various lobe lines. In particular, the specular reflection enhancement was clearly visible; the brightest, specular line overlapped with the entry hole for the laser beam (the black dot in the top panels of Fig. 5). Also, for the shorter antenna the calculated angular width of the lobes was much larger than that for the longer one, in agreement with the experimental maps shown in the top panels. To quantify this, we directly compared the experimental and calculated intensity profiles in Figure 5c, along the line x indicated in Figure 5a. Apart from the broad, diffusive scattering background visible in the experimental profile (solid line), the intensity maxima positions and their broadening was essentially identical to that calculated (dashed line) from the radiation map (inset). Thus, a quantitative agreement between the theory of thin antennae and the experiment was demonstrated, without any adjustable parameters. We have confirmed that the excellent agreement between theory and experiment, as shown in Figure 5, persists for various angles of incidence and radiation wavelengths, and nanotubes of intermediate length.

The observed broadening of the intensity peaks was not caused by nanotube length fluctuations, because of the agreement shown in Figure 5c, and the clearly visible fine structure to the right of the specular line in Figure 5d. SEM pictures of the nanotube arrays confirmed that the nanotubes in these arrays have uniform lengths, with the relative standard deviation from the mean of less than 15 %. Similarly, the observed broadening was not caused by the finite conductivity of the nanotubes since in the calculations we have assumed infinite conductivity. This broadening is, rather, an antenna effect, and can be easily understood in terms of the multisegment interference picture, discussed earlier in this paper. In this picture, the angular lobe width was defined by the angles at which destructive interference (minima) occurred, on each side of the constructive interference maximum. The angular density of the lobes increased with increasing antenna length, as a greater number of current segments contributed to the interference.

The visible antenna effect opens new avenues for light processing in nanomaterials, based on radio technology analogues. For example, one can envision a circuit in which the excited antenna currents can be processed, for example, rectified, amplified, switched on or off, et cetera. In particular, one might realize the concept of a rectenna, the light analogue of the crystal radio, that is, an antenna attached to an ultrafast diode. This could lead to a new class of light demodulators for optoelectronic circuits, or to a new generation of highly efficient solar cells. One could also envision phased arrays of light antennae, enabling a controlled interference of the emitted radiation. Also, since fields are enhanced in the vicinity of antennae, embedding antennae in a nonlinear medium will enhance various nonlinearities. Nanoantennae can also be used as interfaces for various plasmonic devices. In fact, antennae can be fabricated from metals with low plasma frequencies, such as gold or silver, drastically changing their response characteristics.

In conclusion, we have demonstrated that a single multiwall carbon nanotube acts as an optical antenna, whose response is

 © 2007 WILEY-VCH Verlag GmbH & Co. KGaA, Weinheim

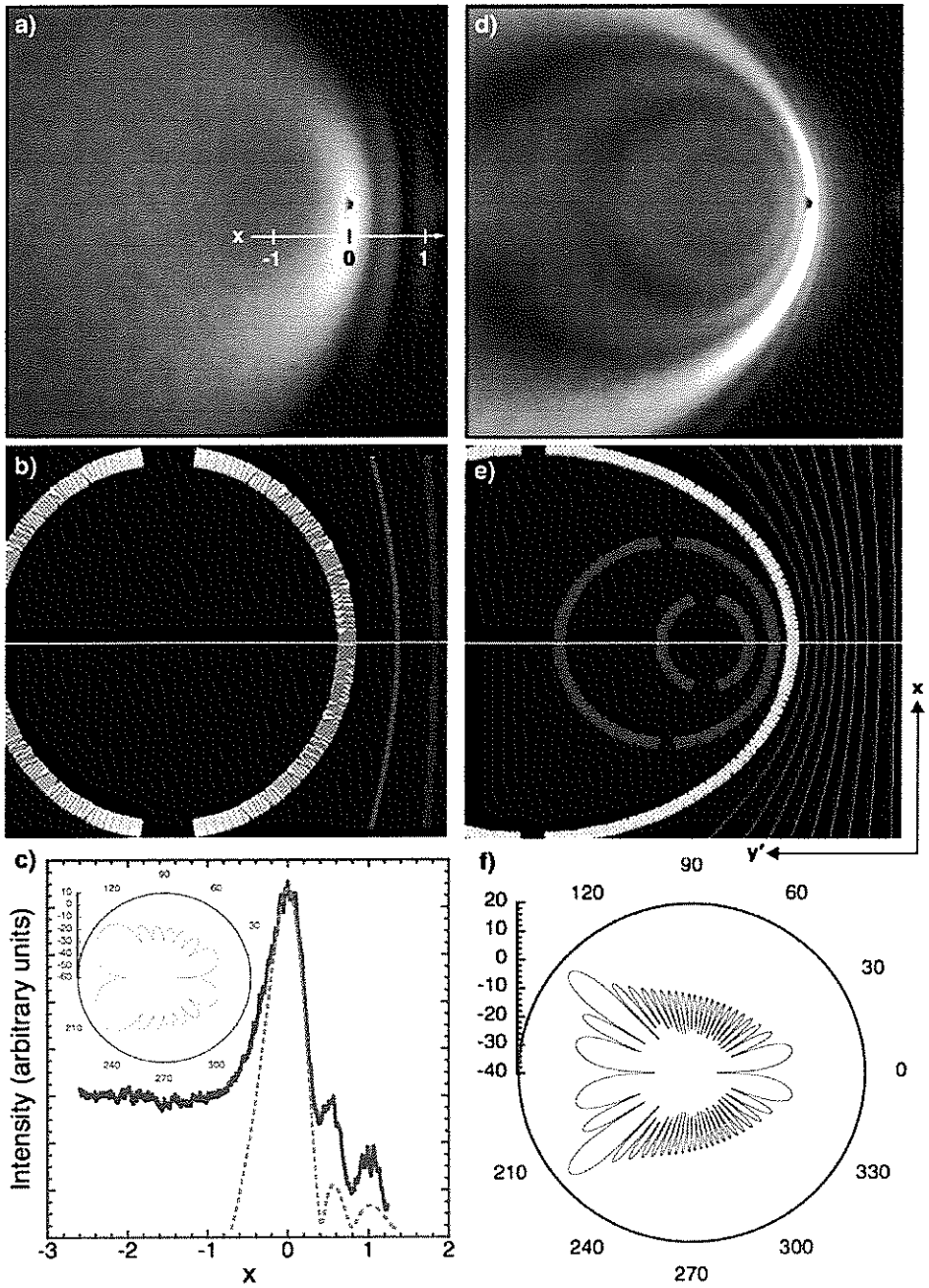

Figure 5. A comparison of the measured (a, d), and calculated (b, e) radiation maps for the nanotubes of Figure 3b and f: (a) and (b) for $l \sim 850$ nm, and (d) and (e) for $l \sim 3.5$ μm. The light wavelength is $\lambda = 543.5$ nm, and the angle of incidence is $\theta_i = 40°$. The corresponding calculated free-standing antenna radiation patterns are shown in the bottom panels (inset in c and (f)) (in decibels, i.e., the $\log_{10}$ of the ratio of the incident power to the emitted power). Each pattern was used to calculate the lobe angles for the corresponding middle panel maps. c) The experimental and calculated intensity profiles, taken along the line x indicated in Figure 5a.

fully consistent with conventional radio antenna theory. We show that the radiation pattern is cylindrically symmetric about the axis of symmetry, and is characterized by a multilobe pattern, which is most pronounced in the specular direction. A quantitative agreement between our theory, simulations, and experiments has been achieved, without any adjustable parameters. Numerous applications are possible based on these optical nanoantennae.

© 2007 WILEY-VCH Verlag GmbH & Co. KGaA, Weinheim

Experimental

MWCNTs were grown using the plasma enhanced chemical vapor deposition (PECVD) technique [17]. Corning 1737 aluminosilicate glass substrates, 25 mm× 25 mm, were first sputter-coated with a thin layer of 15 nm Cr by magnetron sputtering, to obtain a conductive but still transparent layer. The PECVD nanotubes were grown on randomly distributed Ni nanoparticles, which were deposited electrochemically [18]. Briefly, the Cr-coated substrate was used as a cathode in an electrolytic bath, with an aqueous solution of 0.01 M $NiSO_4$ and 0.01 M H_3BO_4 as the electrolyte, and a graphite electrode as an anode. The deposition area was 15 mm× 15 mm, and the spacing between the electrodes 15 mm. The optimal Ni particle dispersion was obtained at 2 mA dc current, and 2.2 s deposition time. The nanotubes were grown in a hot filament PECVD system. A base pressure of 10^{-6} torr (1 torr = 133.322 Pa) was obtained before introducing acetylene and ammonia (40:160 sccm) into the system. The growth process was performed at 40 torr, for 8 min, yielding 5–6 μm long MWCNTs. The substrate temperature was kept below 660 °C.

Received: May 31, 2006
Revised: October 10, 2006

[1] Y. Wang, K. Kempa, B. Kimball, J. B. Carlson, G. Benham, W. Z. Li, T. Kempa, J. Rybczynski, A. Herczynski, Z. F. Ren, *Appl. Phys. Lett.* **2004**, *85*, 2607.
[2] M. S. Dresselhaus, *Nature* **2004**, *432*, 959.
[3] F. E. Terman, *Radio Engineering*, McGraw-Hill, NewYork **1947**.
[4] J. A. Stratton, *Electromagnetic Theory*, McGraw-Hill, New York **1941**.
[5] C. A. Balanis, *Antenna Theory: Analysis and Design*, Wiley, New York **2005**.
[6] K. Fujimoto, A. Henderson, K. Hirasawa, J. R. James, *Small Antennae*, Wiley, New York **1988**.
[7] G. Burke, *Numerical Electromagnetics Code*, NEC-4.1D, Lawrence Livermore National Laboratory, http://www.nec2.org/ (accessed November 2006).
[8] G. Y. Slepyan, S. A. Maksimenko, A. Lakhtakia, O. Yevtushenko, A. V. Gusakov, *Phys. Rev. B* **1999**, *60*, 17 136.
[9] G. W. Hanson, *IEEE Trans. Antennas Propag.* **2005**, *53*, 3426.
[10] G. W. Hanson, *IEEE Trans. Antennas Propag.* **2006**, *54*, 76.
[11] P. J. Burke, S. Li, Z. Yu, arXiv:cond-mat/0408418 .
[12] G. Ya. Slepyan, M. V. Shuba, S. A. Maksimenko, A. Lakhtakia, *Phys. Rev. B* **2006**, *73*, 195 416.
[13] J. A. Stratton, L. J. Chu, *J. Appl. Phys.* **1941**, *12*, 230.
[14] P. Moon, D. E. Spencer, *Field Theory for Engineers*, Van Nostrand Reinhold, New York **1961**.
[15] J. D. Jackson, *Classical Electrodynamics*, 3rd ed., Wiley, New York **1998**.
[16] The mirror image effect occurs only if the response of the electrons in the mirror is sufficiently fast, i.e., the working frequency is well below the plasma frequency of the mirror metal. This was the case in our experiment, since the plasma frequency of Cr is in UV.
[17] Z. F. Ren, Z. P. Huang, J. W. Xu, J. H Wang, P. Bush, M. P. Siegal, P. N. Provencio, *Science* **1998**, *282*, 1105.
[18] Y. Tu, Z. P. Huang, D. Z. Wang, J. G. Wen, Z. F. Ren, *Appl. Phys. Lett.* **2002**, *80*, 4018.

 © 2007 WILEY-VCH Verlag GmbH & Co. KGaA, Weinheim